ADVANCING EARTH AND SPACE SCIENCES

JAMES | Journal of Advances in Modeling Earth Systems®

RESEARCH ARTICLE
10.1029/2023MS003621

Key Points:

- A diffusion limiter—minVAR—was added to the linear basic advection scheme and found to eliminate numerical diffusion completely
- The minimum variance property of minVAR makes the new method optimal for advection of independent tracers as well as correlated ones
- minVAR establishes a unique one-to-one correspondence between points along a Lagrangian trajectory and their mapping to the Eulerian grid

Correspondence to:

R. McGraw,
rlm@bnl.gov

Citation:

McGraw, R., Yang, F., & Fierce, L. M. (2024). Preserving tracer correlations in moment-based atmospheric transport models. *Journal of Advances in Modeling Earth Systems*, *16*, e2023MS003621. https://doi.org/10.1029/2023MS003621

Received 1 MAR 2023
Accepted 25 FEB 2024

Preserving Tracer Correlations in Moment-Based Atmospheric Transport Models

Robert McGraw[1], Fan Yang[1], and Laura M. Fierce[2]

[1]Environmental and Climate Sciences Department, Brookhaven National Laboratory, Upton, NY, USA, [2]Atmospheric Sciences and Global Change, Pacific Northwest National Laboratory, Richland, WA, USA

Abstract A linear non-diffusive algorithm for advective transport is developed that greatly improves the detail at which aerosols and clouds can be represented in atmospheric models. Linear advection schemes preserve tracer correlations but the most basic linear scheme is rarely used by atmospheric modelers on account of its excessive numerical diffusion. Higher-order schemes are in widespread use, but these present new problems as nonlinear adjustments are required to avoid occurrences of negative concentrations, spurious oscillations, and other non-physical effects. Generally successful at reducing numerical diffusion during the advection of individual tracers, for example, particle number or mass, the higher-order schemes fail to preserve even the simplest of correlations between interrelated tracers. As a result, important attributes of aerosol and cloud populations including radial moments of particle size distributions, molecular precursors related through chemical equilibria, aerosol mixing state, and distribution of cloud phase are poorly represented. We introduce a new transport scheme, minVAR, that is both non-diffusive and preservative of tracer correlations, thereby combining the best features of the basic and higher-order schemes while enabling new features such as the tracking of sub-grid information at arbitrarily fine scales with high computational efficiency.

Plain Language Summary A long-standing challenge for the representation of aerosols and clouds in atmospheric models is to properly transport particles in space using higher-order advection schemes. These schemes have less numerical diffusion than the simple basic scheme, but cannot maintain the physical relationship between particle number and mass that needs to be simulated correctly for better understanding of aerosol-cloud-turbulence interactions either in a laboratory-scale cloud chamber or at larger atmospheric scales. The present advection scheme (minVAR, short for minimum variance) introduces a diffusion limiter, under the idea that achieving minimal spatial variance on an Eulerian grid implies maximal resolution and—it turns out - complete elimination of numerical diffusion. By preserving tracer correlations and eliminating numerical diffusion, *minVAR* includes the best features of the simple basic and higher-order schemes. This innovation resolves the two-moment limitation, a necessary first step toward the high-fidelity, multi-moment, multi-scale representation of aerosols and clouds in atmospheric models. Moments, because they are so strongly and nonlinearly correlated, provide an excellent example of correlation failure and serve to focus the present study. That said, there is no reason to suggest that the methods developed here would be inapplicable to other correlated tracer sets.

1. Introduction

The present study was motivated by the need to preserve correlations between interrelated tracers throughout the advection process as it is represented in Eulerian models. Such correlations affect the sequences of radial moments used to track particle size distributions, the main focus of the present study, apportionment of reactive chemical species affecting aerosol composition and mixing state, and tracking of cloud phase. Indeed, the nonlinear correlations between coupled chemically reacting species in the atmosphere (Lauritzen et al., 2015) and the evolution of particle moments and their chemical precursor concentrations in a continuously stirred-tank aerosol reactor (McGraw & Saunders, 1984) are remarkably similar.

Basic linear advection is sometimes referred to as donor-cell as the advected quantity streams from the upwind cell (the donor) into the cell to be updated (van Leer, 2006; Zalesak, 1979). While the basic scheme rigorously preserves tracer correlations, it is highly diffusive, finding application limited mainly to the simulation of laboratory- and industrial-scale reactors and other systems where high-resolution grids and fine time stepping can affordably be used. Specifically, basic linear advection is deemed too diffusive by the atmospheric modeling community for use with the coarse grids applied at regional to global scales. Instead, higher-order finite-differencing approaches are in widespread use. Examples include the Bott scheme, based on polynomial interpolation of concentrations in neighboring grid cells (Bott, 1989a, 1989b), the slopes method, which preserves normalization and first-order spatial moments (Russell & Lerner, 1981), and its successor the second-order moments (SOM) advection scheme, which conserves normalization, and first and second-order spatial moments (Prather, 1986). The higher-order schemes do an excellent job reducing numerical diffusion during the advection of independent tracers, but were never designed to preserve correlations between the tracers from an interrelated set. Moreover, the higher-order schemes are prone to numerical artifacts that can include failure to preserve positivity, monotonicity, and stability. Nonlinear fixes can serve to reduce these artifacts, but such modifications only worsen the tracer correlation problem, increase code complexity, and reduce computational speed.

Sources of the failure to preserve physically based correlations between the lower-order radial moments of a particle population were analyzed by Wright (2007) and attributed largely to the fact that the higher-order advection schemes track spatial gradients that differ for different moments, resulting in dispersion, unphysical size distributions, and corruption of moment sets. Wright examined moment failures for the Bott (1989a, 1989b) and SOM (Prather, 1986) advection schemes using ensembles of 10^4 test cases spanning a range of initial conditions and transport velocities. The Prather scheme performed somewhat better in this regard, but both gave rise to unphysical moment sets at frequencies $\geq 0.7\%$. The problem is not limited to moments. For example, when three species initially with constant sum were advected separately in a one-dimensional constant velocity flow, local errors in the sum ranged from order 10% and up to 30% when cloud-like interactions were considered (Ovtchinnikov & Easter, 2009). Related issues involving mixing and unmixing of two or more tracers, three or more tracers summing to a constant, and the preservation of nonlinear relations (e.g., shape preservation) when using higher-order transport schemes have also been evaluated (Lauritzen & Thuburn, 2012). The aforementioned limitations have huge impact on the representation of aerosol and cloud properties and processes in atmospheric models. They are largely responsible for two-moment aerosol and cloud microphysical schemes, and modal methods currently limited to tracking aerosol number and mass while having to prescribe variance, remaining state of the art. As a result, much of the process-level understanding gained through laboratory and field measurements remains underutilized due to the limited capacity of the models to absorb it.

There have been a few attempts, none entirely successful, aimed at correcting corrupted moment sequences (McGraw, 2007, 2012; Ovtchinnikov & Easter, 2009; Wright, 2007). The present study shifts focus from correcting miscalculated moment sequences produced by the higher-order schemes to limiting numerical diffusion in the basic scheme. This paper was motivated in part by our recent convective cloud chamber study (Yang et al., 2022), which employed a second-order advection scheme and a two-moment cloud microphysical scheme limited to tracking particle number and mass. The new approach introduces a diffusion limiter for the basic scheme, with the idea that achieving minimal spatial variance on Eulerian grids achieves maximal resolution and elimination of numerical diffusion. By preserving tracer correlations and eliminating numerical diffusion, minVAR, short for minimum variance, blends the best features of the basic and higher-order schemes in a way that circumvents the two-moment limitation, thereby allowing for high-fidelity (here multi-moment) representations of aerosols and clouds in atmospheric models.

Section 2 gives a brief preview of the proposed scheme, minVAR, and its comparison to two others, the basic and SOM schemes. Section 3 focuses on methods, introducing optimization theory in the form of an intuitive linear program (LP) to develop minVAR's minimal spatial variance solutions on an Eulerian grid. This is followed by presentation of a closed-form analytic solution for rectangular grids that is computationally faster and fully LP-equivalent. Section 4 focuses on applications. Calculations illustrate the encoding of arbitrarily fine scale features from a spatially dispersed particle cloud onto the coarse grid, while tracking such features at scale with particle-by-particle resolution. A sparse, four-point adaptive quadrature representation of the cloud is also presented. Most importantly, it is shown that contributions to spatial variance from *physical* processes add linearly to minVAR and are (to within numerical precision) separable from it. In other words the two variances, one inherent to the mathematical representation of points on a grid (Section 3), the other physical (Section 4), can be separately identified and individually tracked. Finally, minVAR is applied (Section 5) to the advection of interrelated tracer sets from an external mixture of three distinct aerosol types following a test case introduced by Wright (2007). Recovery of each aerosol type at any stage of the calculation is obtained by least-squares projection onto the

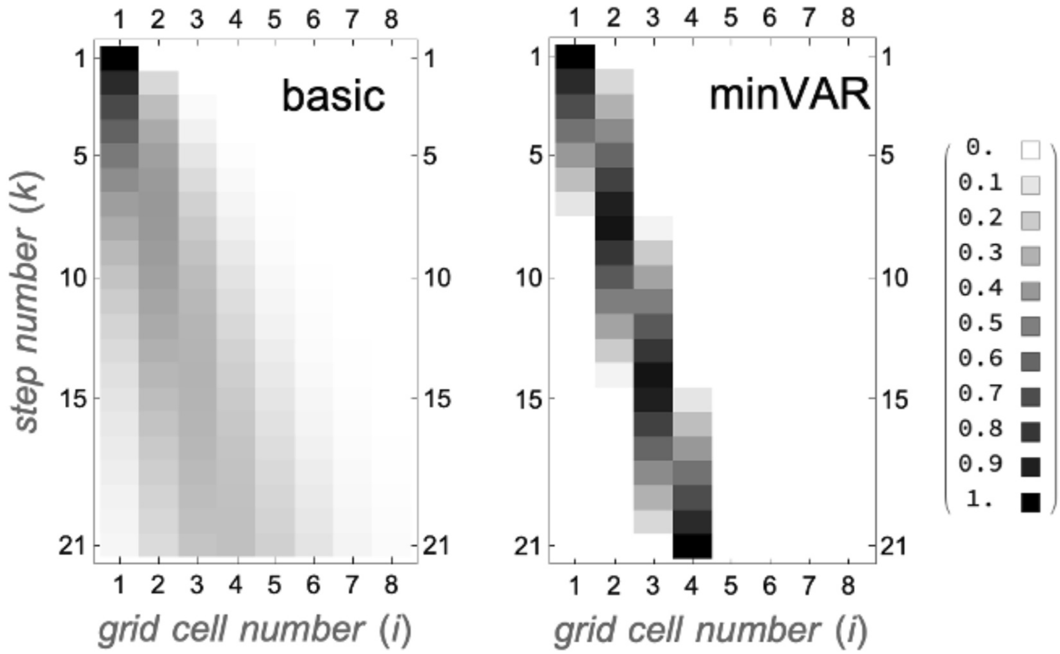

Figure 1. Comparing results from the advection of a single pulse according to the two linear advection schemes. Initial condition: Grid cell 1 filled, others empty. The figure shows results through 20 advection steps with wind direction to the right and $c = 0.15$. Left panel, basic linear scheme. Right panel, minVAR scheme with the new LP diffusion limiter in place. Distributions are normalized to unity with grayscale values indicated in the legend.

vector space spanned by the identifying moment sequence vectors, one for each aerosol type, with zero error residual. Section 6 presents a summary and discussion of the new approach.

In response to reviewer comments, an Appendix has been added that demonstrates versatility of minVAR's LP formulation through its application to reversible shear flow and hemispheric-scale orthographic projection of flow over the northern pole.

2. Preview of minVAR and Comparison With the Basic Linear and SOM Advection Schemes

This section presents a graphical preview of minVAR showing similarities and contrasts between it and the basic and SOM schemes. Details of how minVAR works are introduced in Section 3.

2.1. Advection of a Pulse

Consider the advection of a pulse, consisting initially of a unit amount of tracer material in a single grid cell in a constant velocity one-dimensional flow. Assuming a uniform grid for simplicity, let x_i denote the center of the ith cell, t_n the nth timestep, ΔX the cell width, and $\Delta t = t_{n+1} - t_n$. The Courant number is set at:

$$c = \frac{u\Delta t}{\Delta X} = 0.15, \tag{1}$$

where u is wind speed in the positive x direction. For rational Courant numbers and non-diffusive advection, the perfect-shift property is encountered after an integer number of grid spacings, resulting in exact pulse recovery. For example, for $c = 0.15$, an integer shift of 3 grid spacings is obtained after 20 time steps ($20 \times 0.15 = 3$) as illustrated, in the mean, for the basic scheme, and with exact pulse recovery for the non-diffusive, non-dispersive minVAR scheme in Figure 1.

Density profiles in the basic scheme follow a normalized Bernoulli distribution having mean travel distance $\mu_1(n) = nc$, with $\mu_1(0) = 1$ in the present example, and variance, $\mathrm{var}_x = nc(1 - c)$. n is the number of completed

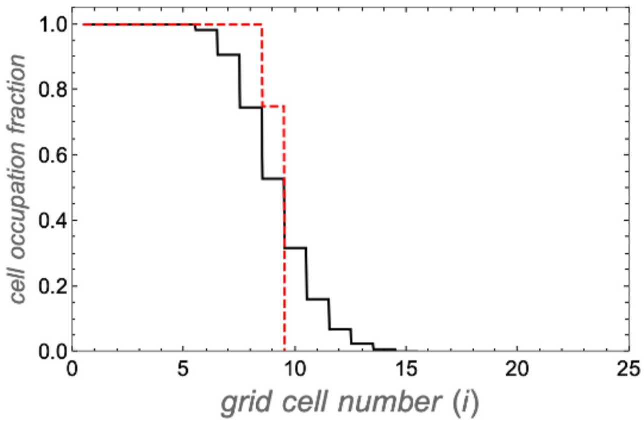

Figure 2. Comparing results from advection of a tracer front. Initial condition: Grid cells 1–5 filled others empty. Results after 25 advection steps with replacement from the left. Curves: Linear advection with (dashed), and without (solid) the minVAR diffusion limiter in place. Both curves average to give the exact travel distance of the front, equal to 3.75 cell widths for $c = 0.15$. After multiples of 20 advection steps using minVAR, the initial step-front (not shown) is exactly reproduced.

advection steps such that $n = k - 1$ for step number k as plotted in Figure 1. With increasing n, the Bernoulli distribution rapidly approximates a normalized Gaussian having these same formulaic values for mean and variance (Chandrasekhar, 1943). The minVAR solution has the same mean $\mu_1(n) = nc$, and an analytic expression for its variance is developed in Section 3. The minVAR solution exhibits exact pulse recovery at $n = 20$ ($k = 21$) and an evenly split pulse of maximal minVAR between grid cells 2 and 3 at $n = 10$ ($k = 11$). This pattern repeats indefinitely.

The exact position after n completed advection steps such that, $\mu_1(n)$, is given correctly in both linear schemes by the centroid of the distributions shown in Figure 1. From exact pulse recovery seen in the figure it is evident that minVAR is completely non-diffusive and unconditionally stable (as exact pulse recovery is repetitive with successive multiples of $20n$). Moreover the minVAR distributions are reversable with reversal of wind direction, yielding recovery of the original pulse in grid cell 1. This is not the case with the basic scheme as the variance continues its linear increase with n irrespective of changes in wind direction due to the irreversibility of numerical diffusion in the basic scheme. Nevertheless, the centroids of the distributions track perfectly and these are restored to their original values in both schemes.

Figure 2 shows an application to a frontal tracking. The initially sharp front, which results from advection of a train of pulses arriving from the left, serves to illustrate the superposition principal for linear advection schemes, here the diffusive basic and non-diffusive minVAR schemes, solid and dashed histograms, respectively.

Figure 3a shows a direct comparison of the minVAR and SOM advection results after 70 advection steps for the same initial unit pulse as Figure 1. The minVAR solution, dashed, is an evenly split pulse of maximal minVAR between grid cells 11 and 12 after an average travel distance of 10.5 cell widths. SOM and minVAR each performed well in this single-tracer test, with SOM showing only a small amount of numerical diffusion in the wings of its histogram. Figure 3b compares the three methods. A rapid and linearly increasing variance with step number is seen for the basic scheme, as expected from the Bernoulli distribution. The solid and dashed curves for SOM and minVAR, respectively, tend to flatten out, indicating that numerical diffusion is controlled in both schemes.

As reversibility and exact pulse recovery after multiples of 20 steps imply, minVAR is non-diffusive. Consequently, the vertical distance between the SOM and minVAR curves of Figure 3b provides a measure of numerical diffusion in the SOM scheme at each advection step. Similarly for the basic scheme, with its much higher and growing level of numerical diffusion, reflected in the difference between the line and minVAR curve. The

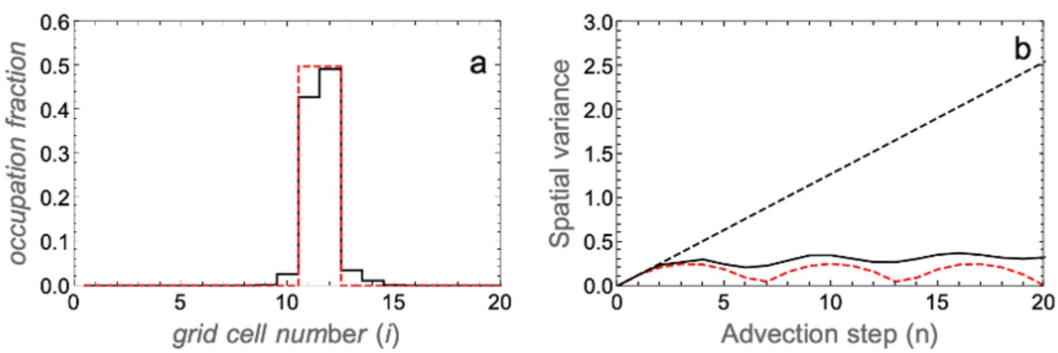

Figure 3. (a) Comparison of pulse shape after 70 advection steps. Histograms of cell occupation fraction for the SOM (solid) and minVAR (dashed) advection schemes. (b) Comparing evolution of spatial variance for the three models from 0 to 20 advection steps: dashed black line (basic scheme), solid curve (SOM), dashed red curve (minVAR). The Courant number is unchanged from Figures 1 and 2. Solid and dashed curves for SOM and minVAR, respectively, tend to flatten out, indicating that numerical diffusion is controlled in both schemes. All three models agree after the first time step, before higher-order SOM gradient terms are evaluated.

Table 1
Linear Program for One-Dimensional Grids of Length n: $LP_{1D}[x(t)]$, $p[i]$ Is the Occupation Fraction of Normalized Material in Grid Cell i Centered at x_i

Minimize variance cost function: $\sum_{i=1}^{n} x_i^2 p[i] - x(t)^2$
subject to:
normalization constraint: $\sum_{i=1}^{n} p[i] = 1$
x-position constraint: $\sum_{i=1}^{n} x_i p[i] = x(t)$
inequality constraints: $0 \le p[i]$ for each i.

minVAR variance is attributed to a purely mathematical effect innate to the Eulerian representation of the coordinates of a zero-dimensional point as it moves across the grid. This requires a minimum of two adjacent grid cells per coordinate to precisely locate the point's position within its home cell, except in special cases of perfect reconstruction where fewer cells are required. Whereas innate variance is solely responsible for shaping the minVAR curve, the SOM scheme carries a vestige of this effect visible in the oscillations with step number seen in the solid curve. A phase shift with respect to the minVAR oscillation is also evident and is due to dispersion in the SOM scheme. Dispersion, together with the conditionally switched-on nonlinearities associated with flux limitation and filling, are largely responsible for destroying tracer correlations in the higher-order models—not numerical diffusion. The basic scheme, though most diffusive of the three, fully preserves tracer correlations.

3. The minVAR Diffusion Limiter for Advection on Eulerian Grids

3.1. Optimization Approach Based on Linear Programming (LP)

The problem of finding minimal variance representations for locating points on a grid has a simple and unique solution obtainable by linear optimization methods. Tables 1 and 2 give linear programs (LPs) for limiting numerical diffusion through constrained variance minimization on one and two dimensional grids. Time-dependent coordinates of a point to be rendered on the grid are indicated as $\{x(t), y(t)\}$. For advection schemes based on finite differencing, calculations are performed on a stencil moved across the grid. For the minVAR advection scheme, finite volumes are employed with calculations carried out on a three by three plaquette of nine grid cells moved across the grid (Figure 4). Solutions in one dimension may be obtained by projecting the plaquette onto the x- or y-coordinate axis, or directly using three-cell central slices parallel to the x- or y- coordinate axis of the plaquette. The method is quite flexible: The code for calculating the right panel of Figure 1, see open research statement, employs eight grid cells along the x- axis ($n = 8$ in Table 1) obtaining numerical values for the entire minVAR grid in a single step. Examples of this flexibility for application of LP to irregular grids, deformation shear, and over-the-pole flow are given in the Appendix.

The two-coordinate LP of Table 2 is a natural extension of the one-coordinate program of Table 1. The number of occupied grid cells in the solution plaquette equals the number of equality constraints (except in special cases of perfect reconstruction where it is less). In one dimension these are the normalization and position constraints and

Table 2
Linear Program for a Two-Dimensional Plaquette: $LP_{2D}[x(t),y(t)]$ $p[i]$ is the Occupation Fraction of Normalized Material in Grid Cell i Centered at $\{x_i, y_i\}$

Minimize variance: $\sum_{i=1}^{9} (x_i^2 + y_i^2) p[i] - (x(t)^2 + y(t)^2)$
subject to:
normalization constraint: $\sum_{i=1}^{9} p[i] = 1$
x-position constraint: $\sum_{i=1}^{9} x_i p[i] = x(t)$
y- position constraint: $\sum_{i=1}^{9} y_i p[i] = y(t)$
zero covariance constraint: $\sum_{i=1}^{9} x_i\, y_i\, p[i] = x(t)\, y(t)$
inequality constraints: $0 \le p[i]$ for each i.

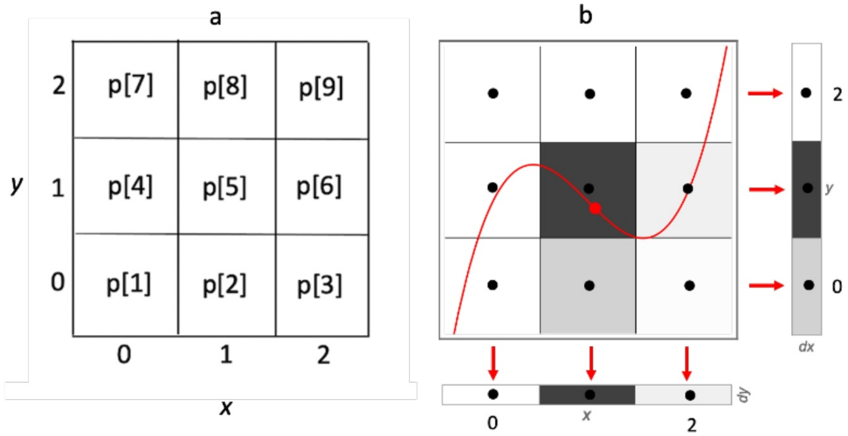

Figure 4. (a) The basic three by three plaquette showing orientation of x- and y- axis and numbering of grid squares. (b) Grayscale representation of densities/occupation number fractions within the plaquette. The red curve depicts a wind trajectory, and a point along that trajectory having coordinates given in Equation 2b corresponding to the centroid of the densities shown. Row and column projections (red arrows) and back projections are discussed in the text.

the solution unique. In two dimensions the zero covariance condition has been added as a fourth equality constraint. This choice yields four occupied grid cells making the solution unique while, at the same time, recovering the results from orthogonal back projections of the 1D x and y solutions (Figure 4). Quadratic terms such as $x(t)^2$, appearing in the cost function, and $x(t)y(t)$ in the covariance constraint, are functions of point-location, which is constant for each call to the program and doesn't affect linearity of the limiter.

Figure 4a shows our convention for the plaquette-square occupation fractions appearing in the program. The nine square centers used in the 2D program take on integer coordinate values $\{x_i\} = \{0,1,2,0,1,2,0,1,2\}$, $\{y_i\} = \{0,0,0,1,1,1,2,2,2\}$, covariance coefficients $\{x_iy_i\} = \{0,0,0,0,1,2,0,2,4\}$, and second moment coefficients $\{x_i^2 + y_i^2\} = \{0,1,4,1,2,5,4,5,8\}$. Solutions are reported using the convention:

$$\mathrm{LP}_{2D}[x(t),y(t)] = \{\mathrm{minVAR},\{p[1],p[2],p[3],p[4],p[5],p[6],p[7],[8],p[9]\}\} \tag{2a}$$

where minVAR is the sought for minimum variance and $p[1]$ thru $p[9]$ are the minVAR grid occupation numbers normalized to unity.

Figure 4b illustrates a specific solution. The lower right corner cells of the plaquette, (cells 2, 3, 5, and 6) contain minVAR's Eulerian representation of the selected point, coordinates of which are indicated by the red marker, along a hypothetical wind trajectory (red curve). Grid occupation numbers are illustrated using the grayscale of Figure 1 with numerical values given in Equation 2b. Cell 3, with $p[3] = 0.014$, appears empty in grayscale as its value is below shading threshold. The trajectory is representative of one that might be input to the advection routine from a separate computational fluid dynamics code or meteorological model. Using coordinates of the selected point as an example, $x = x(t) = 1.07292, y = y(t) = 0.808117$, the solution from Table 2 is:

$$\begin{aligned}\mathrm{LP}_{2D}[x,y] &= \mathrm{LP}_{2D}[1.07292, 0.808117] \\ &= \{0.222667,\{0, 0.177891, 0.0139921, 0, 0.749189, 0.0589279, 0, 0, 0\}\}\end{aligned} \tag{2b}$$

The $p[i]$'s listed in 2b, satisfy the four equality and nine inequality constraints of Table 2, as do many other solutions. What makes this solution unique is that it also minimizes the cost function to give the minimum possible variance representation of the test point's location on the grid. The centroid, or center of mass of the spread, matches the arguments of the LP, its minVAR variance (0.222667) is consistent with the $p[i]$ values listed in 2b. While a single point by itself has no intrinsic variance, its Eulerian representation does. Section 4 generalizes this idea from single points to clouds of points having physical variance added to but separable from minVAR.

Finally it should be noted that central slices from the 2D result recover the 1D forward projections depicted by the arrows in Figure 4b. Specifically, in notation of Equation 2, $\mathrm{LP}_{1D}(x) = \mathrm{LP}_{2D}(x,1)$ and $\mathrm{LP}_{1D}(y) = \mathrm{LP}_{2D}(1,y)$. More

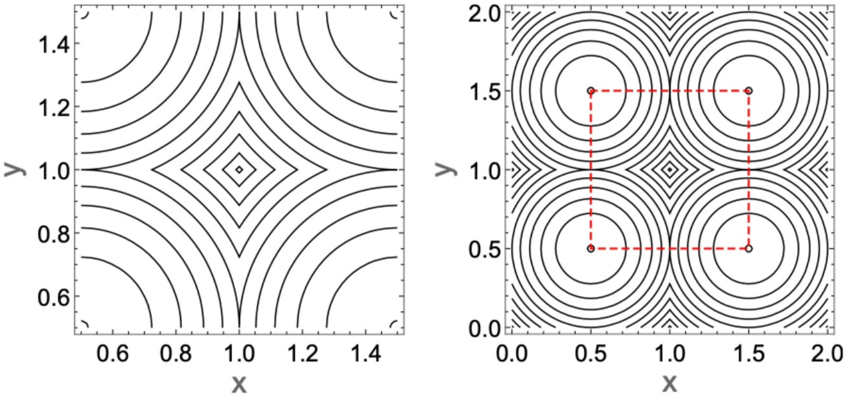

Figure 5. Contours of constant minVAR in 2D. Left, center square of a 9-square plaquette showing contours as a function of point position $\{x, y\}$. Contour values from center to corners are 0.01, 0.05, 0.10, 0.15, 0.20, 0.25, 0.30, 0.35, 0.40, 0.45, 0.499. The first and last entries mark the near center and near corner positions, respectively. Horizontal and vertical lines through the center having coordinates $\{x, 1\}$ and $\{1, y\}$ (not shown) recover variances along the 1D x and y coordinates, as special cases of the 2D solution. Right, stacking of four adjacent cells showing periodicity and continuity across grid cell boundaries. Red square, corners and boundaries of the center square shown on the left. Any point within this 2-cell by 2-cell subregion can be rendered without having to leave the plaquette of Figure 4a.

generally $\mathrm{LP}_{2D}(x,y) = \mathrm{LP}_{1D}(x) + \mathrm{LP}_{1D}(y)$. Results of this type are trivial to prove using a closed-form analytic solution that will now be derived. In contrast to the LP instruction set, the analytic solution, though simpler and much faster to compute, is less intuitive and far less general. Derivation of the analytic result was motivated by the LP-generated contour plots of Figure 5, suggesting the use of LP as a development tool. Both solutions, while numerically equivalent are computationally very different. For these reasons it is of value to retain both derivations for perspective on the new approach.

3.2. LP-Equivalent Analytic Solution and Extension to Three Coordinate Dimensions

The left panel of Figure 5 shows contours of constant minVAR (see caption) for the center square of the plaquette as computed from LP_{2D}. The right panel shows the center square, highlighted in red, imbedded in a larger area of four cells illustrating translational symmetry and toroidal boundary conditions of the underlying grid.

Guided by the radial symmetries exhibited in the minVAR contours of Figure 5, a closed-form analytic solution for computing minVAR was developed and is presented in Table 3. One sees immediately the importance of the corners of each cell, $\{a_x,a_y\}$, serving as centers for the circles of constant minVAR. The lead coefficient on the right for the 1D case, 1/4, is the squared distance from the nearest edge of the grid cell to its center for one coordinate. For two and three coordinates it's the squared distance from the nearest corner of the grid cell to its center. In three dimensions the squared distance corner to center is $(\sqrt{3}/2)^2 = 3/4$. The subtracted term is the squared Euclidean distance from the nearest edge (or corner) to the point being represented.

Table 3 lists the steps used to get Eulerian grid densities beginning with $mV_{1D}(x)$, followed by computation of spatial moments 0, 1, 2 along the coordinate axes, $v1D(x)$ and $v1D(y)$, forward projections of density onto the coordinate axes $p1D(x) \equiv \{px_1,px_2,px_3\}$ and $p1D(y) \equiv \{py_1,py_2,py_3\}$, and finally the back projected densities obtained using an outer product of forward projections. The full result, $fmV_{2D}(x,y)$ in two dimensions, outputs both the minVAR values and back projected cell densities, $bp(x,y)$, following the convention of Equation 2a. $\mathrm{LP}_{2D}(x,y)$ and $fmV_{2D}(x,y)$ give identical results, with the latter showing a 1000-fold gain in computational speed.

Two properties of the minVAR function (mV for short) are worth noting here: (a) the expression for $mV_{1D}(x)$ is easily recovered from $mV_{2D}(x,y)$ upon noticing that the squared vertical distance from a corner to the midpoint of one of its vertical edges is $\Delta_y^2 = 0.25$. Substituting this value into the expression for $mV_{2D}(x,y)$ gives $mV_{1D}(x)$ by the Pythagorean theorem. A similar argument applies to the recovery of $mV_{1D}(y)$. By extension, $mV_{1D}(x)$ is recovered from $mV_{3D}(x,y,z)$ using $\Delta_y^2 = \Delta_z^2 = 0.25$. (b) $mV_{3D}(x,y,z) = mV_{3D}(x + n,y + m,z + l)$, and similarly for lower dimensions, where n, m, and l are any positive or negative integers. This identity, especially useful when

Table 3
Closed-Form Analytic Formulae for minVAR Values and Back Projected Densities

minVAR values in one, two, and three dimensions

1D: $mV_{1D}(x) = 1/4 - \Delta_x^2$ where $\Delta_x^2 = (a_x - x)^2$

2D: $mV_{2D}(x,y) = 1/2 - (\Delta_x^2 + \Delta_y^2)$ $\Delta_y^2 = (a_y - y)^2$

3D: $mV_{3D}(x,y,z) = 3/4 - (\Delta_x^2 + \Delta_y^2 + \Delta_z^2)$ $\Delta_z^2 = (a_z - z)^2$

$\{a_x, a_y, a_z\} = \{\text{Floor}[x] + 1/2, \text{Floor}[y] + 1/2, \text{Floor}[z] + 1/2\}$

Floor$[x]$ gives the greatest integer less than or equal to x

Back-projection formula for plaquette densities in 2D

mat = {{1, 1, 1},{0, 1, 2},{0, 1, 4}} (3 × 3 moment matrix for the reference plaquette of 4a)

$\text{mat}^{-1} = \{\{1, -3/2, 1/2\},\{0, 2, -1\},\{0, -1/2, 1/2\}\}$ (mat inverse)

$v1D(x) = \{1, x, mV_{1D}(x) + x^2\}$ (zeroth, first and second moments, here along x)

$p1D(x) = mat^{-1} \cdot v1D(x)$ (projected densities onto coordinate axes, here x)

Example from Figure 4b: $p1D(1.07292) = \{0, 0.92708, 0.07292\} \equiv \{px_1, px_2, px_3\}$

$p1D(0.808117) = \{0.191883, 0.808117, 0\} \equiv \{py_1, py_2, py_3\}$

back projected plaquette densities **:**

$bp(x,y) = \{px_1py_1, px_2py_1, px_3py_1, px_1py_2, px_2py_2, px_3py_2, px_1py_3, px_2py_3, px_3py_3\} =$

Outer $(p\,1D(y), p1D(x))$

(numerical values in this example are identical to the results from LP shown in Equation 2b)

Full result in 2D: $fmV_{2D}(x,y) = \{mV_{2D}(x,y), bp(x,y)\}$

Full result in 3D: $fmV_{3D}(x,y,z) = \{mV_{3D}(x,y,z), bp(x,y,z)\}$

where $bp(x,y,z) = \{bp(x,y)pz_1, bp(x,y)pz_2, bp(x,y)pz_3\}$. Extension of the outer product to 3 × 3 × 3 = 27 terms to include the vertical coordinate.

working with large grids, is based on the translational symmetry previously described, and captured here by the *Floor* function defined in the table. Such symmetry is analytic proof that minVAR is unconditionally stable in 1, 2, and 3 dimensions.

By inspection, $mV_{3D}(x,y,z) = mV_{1D}(x) + mV_{1D}(y) + mV_{1D}(z) = mV_{2D}(x,y) + mV_{1D}(z)$, etc. Solutions need only be computed in 1D and back projected for results in higher dimension.

The analytic process here is equivalent to time/operator splitting in SOM. On the other hand, minVAR doesn't require time splitting to work in higher dimension. It is applied directly to random points at sub-grid scale in Sec. 4.1, and can equally well be applied to a non-uniform sequence of points along a curved wind trajectory as suggested in Figure 4. In this last sense, minVAR can be viewed as providing a unique one-to-one mapping from Lagrangian trajectories to Eulerian grid densities. Quantities not easily captured by the former approach, for example, sub-grid turbulence and entrainment, may be better captured by mapping to the grid—and vice versa.

For rectangular grids LP and mV are equivalent. LP is more general and will likely have advantages as a development tool in future applications of the method, such as to cases involving the nonuniform grid shapes and areas as illustrated for polar grids and deformation shear flow in Appendix A. Numeric and analytic calculations presented in the following section rely mostly on the closed-form mV and fmV algorithms of Table 3 both for their ease of implementation on rectangular grids and great computational speed.

4. Applications

The previous section described minVAR's Eulerian representation of point singularities located on one, two, and three dimensional grids. These representations, being purely mathematical in nature, are devoid of physical content. That will change with consideration of multi-point physical representations of aerosols and clouds developed at arbitrarily fine sub-grid scales in Section 4.1. Dual LP, equivalently dual minVAR, is introduced to obtain the sensitivity of minVAR values to particle motions across the grid in Section 4.2. Finally, the problem of

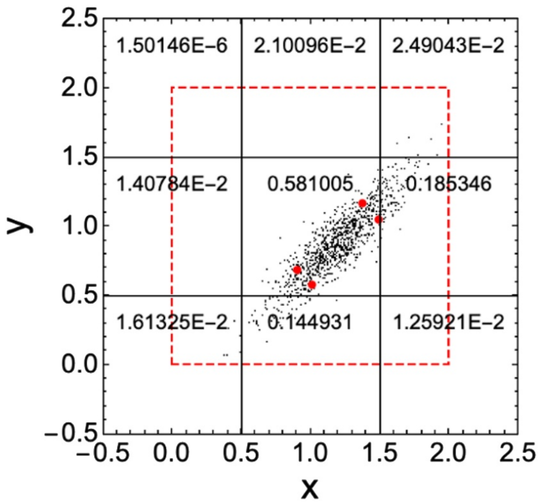

Figure 6. Sampled set of 1000 points from the parameterized binormal distribution of Equation 3a (black dots) and four adaptive quadrature points (red dots) having the same six lower-order moments {normalization, $\langle x\rangle$, $\langle y\rangle$, $\langle xx\rangle$, $\langle yy\rangle$, $\langle xy\rangle$}. The quadrature points have equal weights, ¼ each, and lie at corners of a rectangle representing the ± sigma values of the sampled binormal distribution (Equation 3b). Cell numbering refers to the averaged plaquette values of Equation 6b. The figure illustrates a nice property of minVAR, namely that it enables arbitrarily fine sub-grid scale information to be encoded on a much coarser parent grid.

advecting a mixture of distinct aerosol types, each having its own identifiable sequence of interrelated moments, is described separately in Section 5. Similarities and differences between the minVAR, basic, and SOM schemes in this regard are also discussed.

4.1. Separation and Tracking of Variance From Physical Processes Using minVAR

This subsection illustrates how sub-grid information can be represented in minVAR parametrically or on a particle-by-particle basis, the latter using spatially distributed, multi-point configurations that can represent individual aerosol particles and cloud droplets or sparse representations of their spatial distributions using adaptive quadrature. Such extended systems carry their own physical variance and covariance in addition to their pointwise spatially dependent innate variance contained in minVAR itself. The linearity feature of minVAR allows these different contributions to be tracked separately through multiple grid boxes of volume $\Delta V = \Delta X \Delta Y \Delta Z$ using the methods developed here and in Sec. 4.2.

Figure 6 shows a collection of 1000 particles (black dots) sampled from a binormal distribution having mean, $\{\mu_1,\mu_2\} = \{1.2, 0.88\}$, and covariance matrix elements from Equation 3

$$\begin{pmatrix} \sigma_1^2 & \rho\sigma_1\sigma_2 \\ \rho\sigma_1\sigma_2 & \sigma_2^2 \end{pmatrix} = \begin{pmatrix} 0.0625 & 0.05625 \\ 0.05625 & 0.0625 \end{pmatrix} \tag{3a}$$

where ρ is a number between −1 and 1, here $\rho = 0.9$. The parameters on the left of Equation 3a, generally time dependent, may be tracked directly without sampling the distribution using adaptive sigma-point quadrature (Yoon & McGraw, 2004a, 2004b). The limitation of parameterization, though extremely efficient, is that the distribution shape may morph from binormal to a very different form, necessitating reparameterizations over time. The use of many more points affords much greater accuracy and flexibility in this regard, as does quadrature. Both approaches are remarkably fast, when minVAR is used. Quadrature, with significantly fewer points, is of course much faster. Both particle-by-particle aerosol/cloud tracking and adaptive sigma-point quadrature employ the same sets of lower-order mixed moments, and these evolve over time with closure independent of any parameterized form.

The 1000-point sample from the binormal distribution of Equation 3a has slightly different mean and covariance values due to the random nature of the sampling: $\{\mu_1,\mu_2\} = \{1.19263, 0.872259\}$ and covariance matrix:

$$\begin{pmatrix} \sigma_1^2 & \rho\sigma_1\sigma_2 \\ \rho\sigma_1\sigma_2 & \sigma_2^2 \end{pmatrix} = \begin{pmatrix} 0.0592442 & 0.0530498 \\ 0.0530498 & 0.0598873 \end{pmatrix} \tag{3b}$$

The 1000 particle sample (black points), and its 4-point quadrature representation (red points), shown in Figure 6, have the same six lower-order moments (normalization, mean values, and covariance matrix elements). The sparse quadrature representation is generated in the principal frame and transformed back to the original frame of the sampled distribution using sigma-point quadrature. Here the form of the distribution doesn't matter, only its moments matter. As the 1000 particles evolve spatially over time, so do the quadrature points, which continue to follow the same lower-order moments, independent of how location and shape of the distribution change over time (Yoon & McGraw, 2004a, 2004b). Figure 6 represents what the distribution and its sparse representation might look like at a snapshot in time.

For a single point the difference between minVAR values calculated directly from $mV_{2D}(x,y)$ and from the plaquette densities on the Eulerian grid vanishes. This can be checked using the numbers in Equation 2b, which apply to a single point. Substitution gives:

$$\sum_{i=1}^{9}(x_i^2 + y_i^2)\,p[i\,\} - \left(x(t)^2 + y(t)^2\right) - mV_{2D}(x(t),y(t)) = 0, \tag{4}$$

which is consistent with the physical variance of the point being zero. The averaged minVAR over two or more points no longer equates to the correspondingly averaged back projected densities. The latter is always larger. To demonstrate, it is instructive to look at $fmV_{2D}(x,y) = \{mV_{2D}(x,y), bp(x,y\}$ averaged over the thousand point sample of Figure 6,

$$\langle fmV_{2D}(x,y)\rangle = \left(\sum_{i=1}^{1000} fmV_{2D}(x_i,y_i)\right)/1000. \tag{5}$$

The centroid of the 1000-particle sample, corresponding to the black points of Figure 6, has coordinates $\{\mu_1, \mu_2\} = \{1.19263, 0.872259\}$ and a *physical* variance $(\sigma_1^2 + \sigma_2^2) = 0.0119131$ given by the sum of the diagonal elements of Equation 3b. The aim here is to demonstrate recovery of this physical variance using minVAR. The 1000-point averaging yields averages over the point-by-point minVAR values, $\langle mV_{2D}(x,y)\rangle$, and over the back projected densities $\langle bp(x,y)\rangle$. For the former, averaging over the black points gives:

$$\langle mV_{2D}(x,y)\rangle = \left(\sum_{i=1}^{1000} mV_{2D}(x_i,y_i)\right)/1000 = \langle \text{minVAR}\rangle = 0.30007 \tag{6a}$$

For the latter, averaging over the plaquette densities point-by-point gives:

$$\langle bp(x,y)\rangle = \{0.016, 0.145, 0.0126, 0.0141, 0.581, 0.185, 0, 0.021, 0.025\} \tag{6b}$$

Using these averaged $p[i]$ values from 6b and subtracting the point-averaged minVAR from 6a gives:

$$\left\langle \sum_{i=1}^{9}(x_i^2 + y_i^2)\,p[i] - \left(x(t)^2 + y(t)^2\right)\right\rangle - \langle mV_{2D}(x(t),y(t))\rangle = 0.0119131. \tag{6c}$$

For this calculation we used the higher precision averaged p[i] values given by the entries in Figure 6. Unlike with the single-point case of Equation 4, the left side of Equation 6c is always positive. Here it's value is precisely equal to the physical variance associated with the spatial distribution of points obtained previously from the sampled distribution by summing the diagonal elements of the variance-covariance matrix of Equation 3b. Note that as time evolves numerical values on the right hand sides of Equations 6a and 6b will also evolve, but the general principle of precisely recovering the physical variance by subtraction is unchanged.

Regarding the covariance, note that taking the inner product of the 9-element arrays, $\{xy\} = \{0, 0, 0, 0, 1, 2, 0, 2, 4\}$ and $\langle bp(x,y)\rangle$, and subtracting from this the product of the x- and y- mean values of the 1000-point distribution, gives exactly the covariance of the averaged plaquette densities, 0.0530498 as previously obtained from the sampled distribution by noting its equivalence to the off-diagonal elements of Equation 3b. In this case no subtraction of the averaged minVAR covariance, which vanishes due to the zero covariance condition invoked in Table 2, is required.

Collectively, these features enable the separation and tracking of the physical variance and covariance arising from aerosol and cloud processes that may include dissipation from wind shear and/or physical diffusion associated with turbulent mixing and entrainment, independent of minVAR's innate variance, a mathematical quantity essential to development of the new advection scheme but devoid of physical content. Additionally, each point from the distribution maintains its individual properties recorded in and recoverable from the coarse grid (cf. Figure 6). Summing these together they represent the distribution itself—a nice illustration of the superposition principle that holds for non-dispersive linear models. The 4-point quadrature approximation not only speeds up the calculation, by an additional 30x as compared with the 1000-point calculation, it produces the same numerical values as averaging over the 1000-point distribution itself, shown in Equation 6, as the four adaptive quadrature points track the same spatial moments.

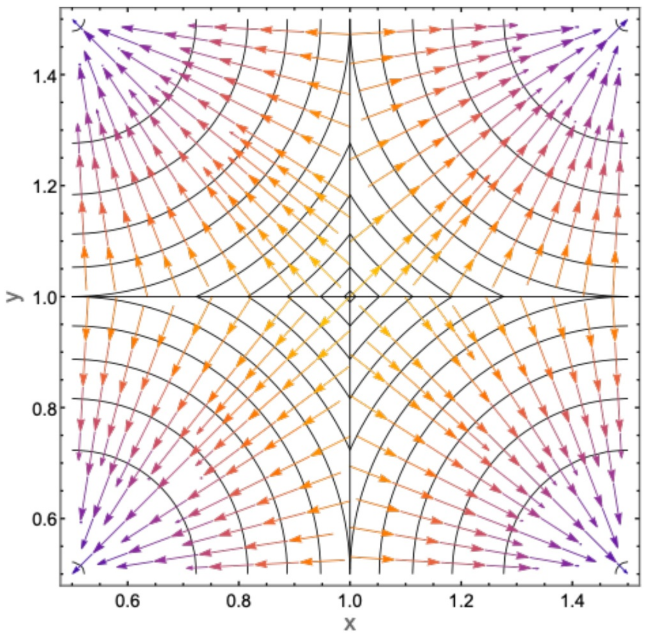

Figure 7. Primal-dual solutions to minVAR. Comparing the primal solution for minVAR (black contours as in Figure 5) with the dual solution for sensitivities (gradient vector field) superposed. Colors represent the vector norm, which is smallest, equal to zero, at the corners (purple) and largest, equal to $\sqrt{2}$ at the center (yellow). Horizontal and vertical lines highlight the four quadrants and symmetries of the minVAR solutions.

Figure 6 suggests a convenient way to assign a unique plaquette to any point on the full grid. As discussed in connection with Figure 5, any point within the 2×2 sub-region highlighted by the dashed perimeter in Figure 6 can be rendered in Eulerian form on the surrounding 3×3 plaquette sharing its center. Conversely, any point outside the red square can be represented only by using a neighboring plaquette. This suggest that any point on the full grid can be rendered simply by overlapping one row or column of neighboring plaquettes such that the 2×2 cell subregions form their own grid. Each point is then identified with the one and only one plaquette whose center coincides with that of the 2×2 cell sub-region containing the point in question. It would be interesting to explore whether this new class of plaquette-based overset composite grids can avoid singularities of the conformal-map-based grids by minimizing expense of introducing overlap (Staniforth & Thuburn, 2012).

4.2. Dual LP and Dual minVAR

Each LP comes with its unique dual program, constructed from it using the same I/O, see for example, (Bazaraa, et al., 2010) for rules of construction. For present purposes, the most important result from the dual LP is sensitivity of the minVAR cost function to changes in location as individual point particles follow wind trajectories across the grid. Figure 7 shows the minVAR contours from Figure 5 superposed with the dual minVAR solution described below.

Analytic solution for the dual: simplicity of the analytic forms for minVAR, evident in Table 3, make it unnecessary to go through the dual LP, as the desired sensitivities are easily obtained directly from the analytic result. Denoting these sensitivities as $v_x = \frac{\partial mV_{2D}(x,y)}{\partial x}$ and $v_y = \frac{\partial mV_{2D}(x,y)}{\partial y}$, and taking derivatives of the expressions in Table 3 gives:

$$v_x = 2(1/2 - x + \mathrm{Floor}[x]) = 2(a_x - x)$$

$$v_y = 2(1/2 - y + \mathrm{Floor}[y]) = 2(a_y - y) \tag{7}$$

for components of the contour gradient vector in 2D. Floor[x] changes discontinuously at integer values of x, a feature responsible for the piecewise parabolic structure of minVAR, seen in the red dashed curve of Figure 3b, and discontinuous changes in v_x and similarly, in 2D, for v_y. The minVAR curves are in fact obtainable by integration over the gradient vector field described by Equation 7. Sensitivity vectors having components given by Equation 7 are plotted using the StreamPlot feature of *Mathematica* in Figure 7 and superposed on the minVAR contours. One sees that the gradient field and minVAR circles are mutually orthogonal to each other. They are in fact each other's dual, reflective of the textbook property that the dual of the dual program gives the "primal" or original program back again (Bazaraa, et al., 2010). From Equation 7 and definition of the sensitivities given above:

$$d\, mV_{2D}(x,y) = v_x dx + v_y dy, \tag{8}$$

which vanishes along the circular contours of constant minVAR. For if r is the radial distance from the nearest corner $\{a_x, a_y\}$, the directional derivative along line $r(\theta)$ has the form:

$$\frac{d\, mV_{2D}(x,y)}{dr} = v_x \sin\theta + v_y \cos\theta \tag{9}$$

where θ is the angle the line makes with the vertical axis. Equations 8 and 9 are equivalent to the result that $dmV_{2D}(x,y)$ vanishes along any circular contour, $dr = 0$. This demonstrates that properties of the primal (here circular contours of constant minVAR centered on the staggered network of cell corners) can be deduced from the conjugate properties of the dual (sensitivities) and vice versa.

Restoring dimensionality to the grid coordinates, x and y, gives the true distances (meters) from the grid origin to $\{x\Delta X, y\Delta Y\}$ where ΔX and ΔY are the actual grid spacings. The time derivative of minVAR is then:

$$d\, mV_{2D}(x,y) = \frac{\partial mV_{2D}(x,y)}{\partial x}\, u\, dt + \frac{\partial mV_{2D}(x,y)}{\partial y}\, v\, dt, \tag{10}$$

where $u = \Delta X dx/dt$ and $v = \Delta Y dy/dt$ are the corresponding wind velocity components taken at each sampled point along a wind trajectory and inputted to the advection algorithm at time intervals dt.

Figure 7 shows primal-dual results for the center grid cell. The gradient vector field for neighboring cells follows the same translational symmetry as the grid itself. The gradient vectors point from the least diffuse state at cell center (minVAR = 0) to the most diffused states located at the cell corners (minVAR = ½ in 2D). Though of purely mathematical origin, the direction these vectors take is the same as would any physical variance increasing with time according to the second law (increased variance corresponding to increased entropy in the physical case). Time-dependent increases in physical variance due to irreversible microphysical and fluid-dynamical processes, such as diffusive mixing from entrainment and energy dissipation from shear, are separable from the minVAR gradients shown in the figure, in much the same way that mathematical and physical contributions to the variance itself were separated in Section 4.1. Development of the most efficient ways to represent dissipative processes in sub-grid models based on this separation will be considered in future studies.

5. Preserving Moment Sequence Correlations During Advection

The testing of tracer advection schemes typically involves the transport of individual tracers in one or two dimensions, often with periodic boundary conditions (Rood, 1987)—a reasonable approach given that the schemes undergoing such testing were never designed to preserve correlations between a sequence of tracers from an interrelated set. The SOM scheme, discussed in Section 2 has been subject to tests of this type including simple clock rotation and pure advection in 2D (Shia et al., 1990). Testing for preservation of correlations between sets of interrelated tracers during advection, has been limited largely to those few papers mentioned in Section 1. Here we apply a test devised by Wright (2007), originally to assess the integrity of correlated moments under vector transport involving one or two lead moments. McGraw (2007) used non-negative least squares (NNLS) (Lawson & Hanson, 1995) to assess the effect of transporting four moments from identifiable sequences associated with each of three distinct aerosol types employed in the test. Not surprisingly NNLS performed better than vector transport using just one or two lead moments, but all of these tests showed levels of moment set reconstruction far from perfect (McGraw, 2007, 2012; Wright, 2007). The goal of the Wright and McGraw studies was to identify and correct corrupted moment sequences. The aim in this section is to showcase minVAR as an entirely new transport algorithm, designed explicitly to preserve tracer correlation, and thereby obviate any need for moment correction.

Wright's correlation test considers an external mixture of three aerosol types each characterized by a unique lognormal distribution and corresponding sequence of four radial moments $\{\mu_0,\mu_1,\mu_2,\mu_3\}$ where $\mu_k = \int_0^\infty r^k f(r)\, dr$. In vector form these sequences are:

$$\begin{aligned} v_1\ (\text{red}) &= \left\{1.0\times 10^6, 30802.2, 9001.71, 24959.3\right\}^T \\ v_2\ (\text{green}) &= \left\{1.0\times 10^4, 10106.2, 260788.0, 1.71832\text{x}10^8\right\}^T \\ v_3\ (\text{blue}) &= \left\{1.0\times 10^3, 151.593, 586.774, 57993.2\right\}^T. \end{aligned} \tag{11}$$

where the superscript T stands for transpose. Colors identify the three aerosol types shown in the histogram plots of Figures 8, 10, and 11. As this a pure advection test case, without microphysics, the moments for each aerosol type, though they mix, ideally remain proportional throughout the simulation. For the initial condition (M_0), 20 grid cells are populated with just one aerosol type in each cell. The types are distributed according to the following 4×20 matrix (Figure 8):

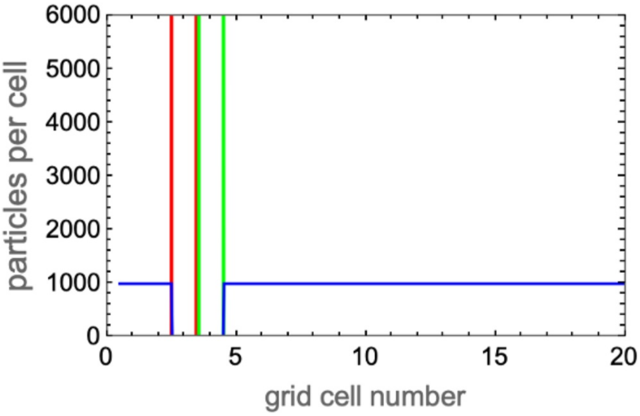

Figure 8. Initial condition for the zeroth moment (particle number) used in the Wright test, Equations 11 and 12. Red is off scale at 10^6, green is off scale at 10^4. Figures 10 and 11 show the evolution of this distribution after 70 advection steps using SOM and minVAR, respectively.

$$M_0 = \{ v_3, v_3, v_1, v_2, v_3, v_3, v_3, v_3, v_3, v_3, v_3, v_3, v_3, v_3, v_3, v_3, v_3, v_3, v_{3,}\ v_3 \}. \quad (12)$$

Advection is carried out using periodic boundary conditions and the wind direction and Courant number are as in Figure 1. Thus with each advection step 15% of the tracers of cell 20 get transferred to cell 1% and 85% stays in cell 20, etc. Throughout the calculation each moment is transported as an independent tracer before going on to the next moment and the results are combined to update M after each step.

Wright's test is now employed to test advection of moments both as independent tracers and for loss of correlation. The four panels of Figure 9 show the advection test applied to each of the four radial moments μ_0,μ_1,μ_2,μ_3 advected separately across the grid as independent tracers. The two histograms in each panel are results for advection using SOM, solid black, and minVAR, dashed red. As with the pulse test comparison of Figure 3a, both models show numerical diffusion well under control.

The quantification of dispersion is more difficult to assess for the tracer mixture than it was for the single-tracer pulse test comparison of Figure 3b. The histogram shapes in Figure 9 tend to differ for each moment. An exception is seen in moments μ_0 and μ_3, which have similar shapes to each other irrespective of whether they were advected by SOM or minVAR. These moments turn out to be spatially shifted from each other by almost exactly one grid spacing — equivalent to the one full cycle shift in phase (seen on multiples of 6 ⅔ advection steps) in Figure 3b. This suggests strong linkages between dispersion, phase shift, and distribution shape. The top row of Figure 3b also shows a nearly constant shift in phase between the two advection schemes whereas the moments μ_1 and μ_2 in the bottom row do not - perhaps due to the non-integer differences in the shift these two moments take.

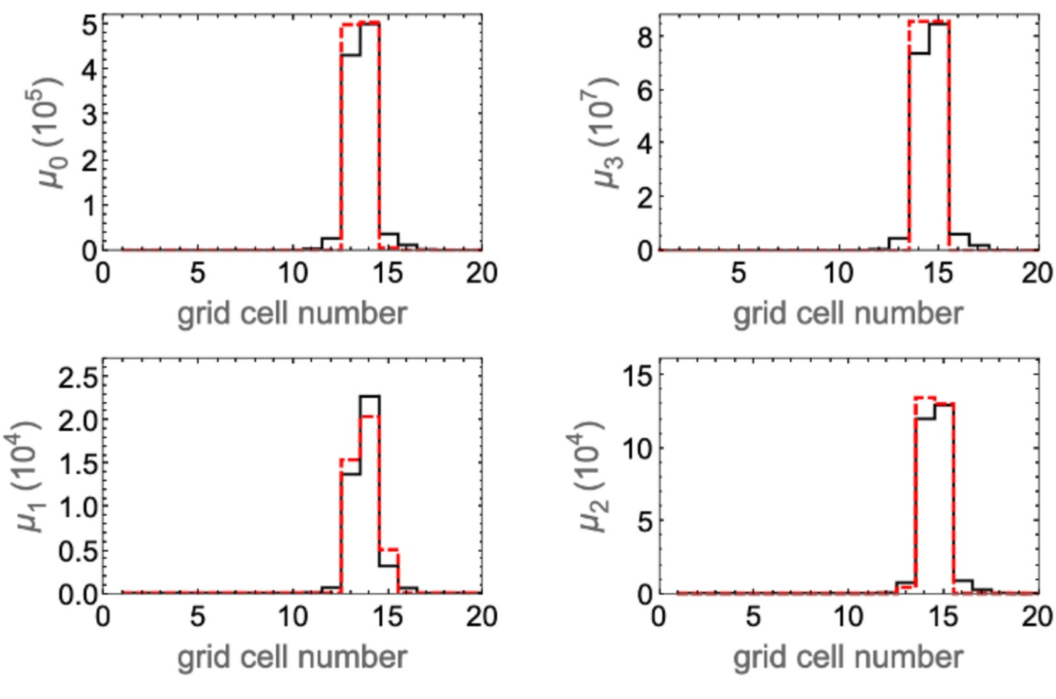

Figure 9. Individual transport of each of the four radial moment tracers under SOM (solid black) and minVAR (dashed red) histograms each representing the full externally mixed aerosol population. Results are shown after completion of 70 advection steps. Upper row: particle number, μ_0, and μ_3, proportional to particle volume. Lower row: μ_1, radial moment, and μ_2, proportional to particle surface area.

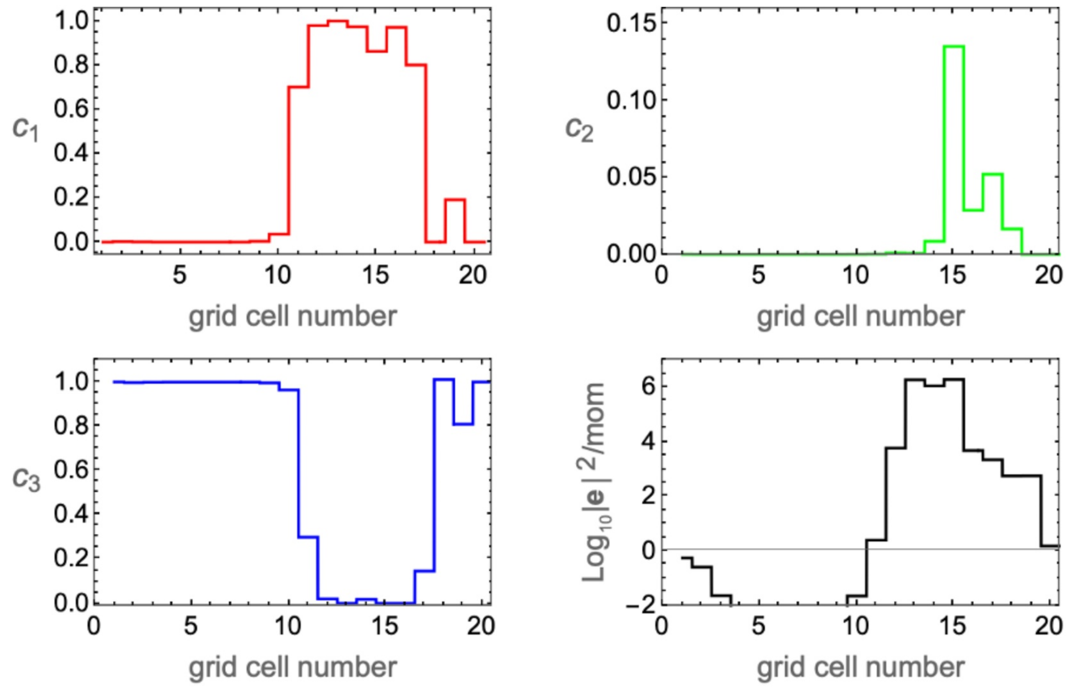

Figure 10. Results from SOM after 70 advection steps. The coefficient distributions, c_1–c_3 refer to use of normalized moments. These were projected from the mixture in each grid cell using NNLS decomposition following McGraw (2007). The lower right quadrant shows distribution of mean squared error per moment obtained on dividing by 4 to average over the 4 moments per column following advection of the original (unnormalized) distributions. The wrap-around effect from period boundary conditions is evident in the panels.

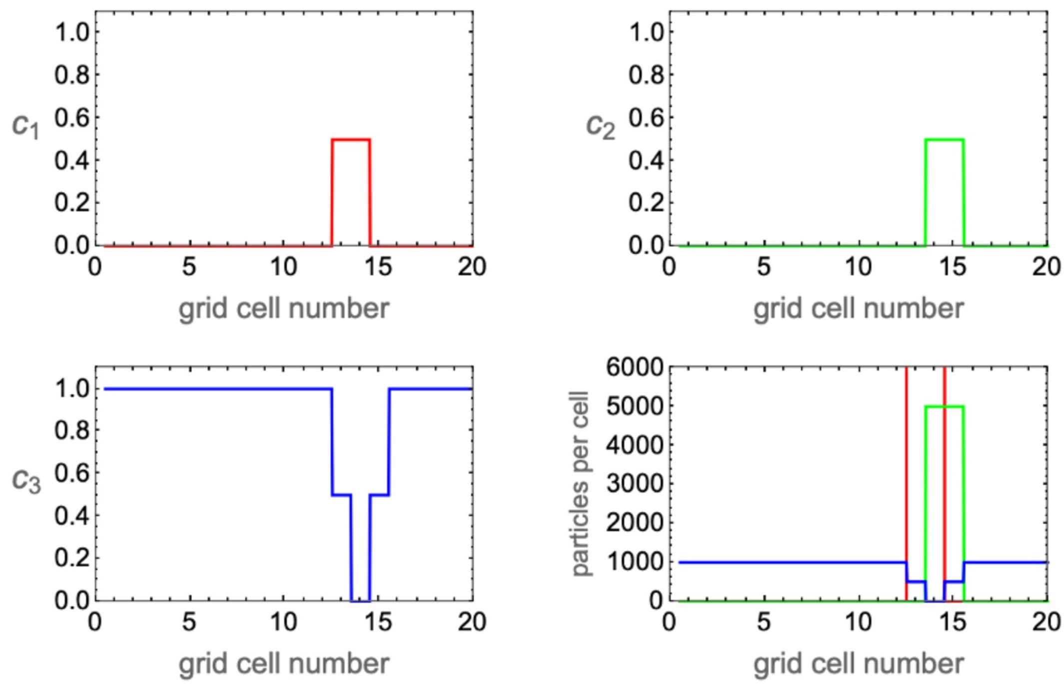

Figure 11. Results from minVAR after 70 advection steps. The coefficient distributions, c_1–c_3 refer to use of normalized moments as in Figure 10. These were projected from the mixture in each grid cell using NNLS decomposition following McGraw (2007), but in this case the pseudoinverse is simpler to use and gives identical results. The lower right panel shows the unnormalized distributions together.

Correlation loss is examined next. This test requires projecting each of the three aerosol types from the advected columns of M_{70}, the updated version of M_0 after 70 advection steps. Let $\mathbf{A} = [\mathbf{v}_1, \mathbf{v}_2, \mathbf{v}_3]$ be the 4 by 3 matrix consisting of the length 4 moment arrays for each of the 3 pure aerosol types as columns, and $\mathbf{b}_j$ the jth column vector of the moments in cell j after any given number of advection steps (here 70). NNLS can be used to do a forensic analysis to project out the different types of aerosol present in each of the columns of M_{70}. Errors due to loss of moment correlation will also be uncovered during this process when higher-order advection schemes are employed. The method, originally used as a way to correct corrupted moment sequences, was applied to SOM previously (McGraw, 2007). Figures similar to those shown in the first row and lower left quadrant of Figure 10 are also given in that paper. NNLS solves the following linear system:

$$\mathbf{A}\ \mathbf{c} = \mathbf{b}_j + \mathbf{e}, \tag{13}$$

obtaining the coefficient vector $\mathbf{c} = (c_1, c_2, c_3)^{\mathrm{T}}$ that minimizes the Euclidean norm of the error residual, $\mathbf{e}$. Use of NNLS ensures non-negative coefficients c_i.

Ideally, as aerosols and their moment sequences mix but are not changed in the test, error residuals should vanish to give the fraction of each aerosol type present in each cell. Such is the case for the two linear models, basic and minVAR, and the aerosol composition in each cell is completely resolved into the original aerosol types ($\mathbf{e} = 0$):

$$\mathbf{b}_j = \mathbf{A}\ \mathbf{c} = c_1\ \mathbf{v}_{1+}c_2\mathbf{v}_2 + c_3\ \mathbf{v}_3. \tag{14}$$

For linear systems, where Equation 14 applies, a simpler least-squares error test, based on the pseudoinverse of $\mathbf{A}$, suffices to do the decomposition (Strang, 1988) and both NNLS and pseudoinverse gave identical results.

With higher-order advection schemes negative coefficients were sometimes found to occur when applying the pseudoinverse and NNLS was used instead to ensure non-negativity. The R, G, and B histograms of Figure 10 plot the coefficients, c_1, c_2, and c_3, respectively, for each column of M_{70}, as obtained from advection using SOM and decomposition using NNLS. The coefficients themselves are seen to be dispersed over an unphysically wide swath of the grid. This itself, supported by the significant level of mean-squared error seen in the lower right panel, is indicative of loss of moment correlation.

A test for unphysical moment sequences was also carried out for each of the 20 columns of M_{70} and none were found. It should be noted, though, that finding unphysical moments in even a single column of the 20 would be a 5% failure rate, whereas Wright reported failure rates closer to 1% for SOM, based on his analysis of an ensemble of 10^4 test cases (Wright, 2007). The moment sequence viability test is as follows: A necessary and sufficient condition for physicality of a moment sequence is that certain Hankel-Hadamard determinants constructed from the moments be positive (McGraw, 2012; Shohat & Tamarkin, 1943). For physicality of the sequence $\{\mu_0, \mu_1, \mu_2, \mu_3\}$, the requirement is that each of the four elements of the following determinant sequence be positive:

$$\left\{\mu_0, \begin{vmatrix} \mu_0 & \mu_1 \\ \mu_1 & \mu_2 \end{vmatrix}, \mu_1, \begin{vmatrix} \mu_1 & \mu_2 \\ \mu_2 & \mu_3 \end{vmatrix}\right\} \geq 0\,. \tag{15}$$

Figure 11 shows results from a similar calculation, with M_{70} computed from the same initial condition, M_0 of Figure 8, but updated at each time step according to the minVAR scheme. The R, G, and B histograms of Figure 11 again show the coefficients, c_1, c_2, and c_3 plotted for each grid cell. In this case there is minimum possible coefficient dispersal over the grid and zero mean square error ($\mathbf{e} = 0$) indicative of full moment sequence preservation. Consistent with linear superposition, the red and green fractions each sum to unity as each occupied single grid cells, 3 and 4 respectively, at $t = 0$. The blue fractions sum to 18 as blue occupied the 18 remaining cells initially (Figure 8). The lower right quadrant shows results for the original (unnormalized) distributions. Red is off scale at 5.0×10^5. Extension to 80 or any other multiple of 20 advection steps would show a shifted but perfectly reconstructed version of the initial condition. The last finding is especially important; it shows that both shape-preservation on individual tracers and sum preservation, not just for particle number, μ_0, but for each of the other three moments μ_1–μ_3, is achieved using minVAR. Advection was carried out using the same periodic boundary conditions as in Figures 9 and 10 and under the same wind direction and Courant condition, $c = 0.15$.

6. Summary and Discussion

Key features of the minVAR limiter discussed in this paper may be summarized as follows: (a) As applied to the basic linear advection scheme, minVAR was found to eliminate numerical diffusion completely while preserving the best features of that scheme including linearity and freedom from dispersion (Section 2). The latter feature, achieved by not having to reference higher-order gradients, which will typically differ for different tracers of an interrelated set, is key to the preservation of tracer correlation (Section 4). (b) The minimum variance property of minVAR makes the new method optimal for advection of independent tracers as well as correlated ones (cf. Figures 3 and 9 for a comparison with SOM in this regard). As minimal spatial variance implies maximal spatial resolution, this feature suggests minVAR, which preserves pulse resolution to no more than two grid spacings per coordinate throughout the course of a simulation, could well replace the more slowly convergent basic scheme for modeling even at the fine scales of laboratory and engineering simulation. (c) As a point-by-point method, minVAR establishes a unique one-to-one correspondence between points along a Lagrangian trajectory and their representation on an Eulerian grid. This direct correspondence allows the best features of Lagrangian and Eulerian methods to reinforce each other in simulations. (d) The extension from single points to multi-point representations of aerosol and clouds exhibits a rigorous and complete separation of physical variance from the innate mathematical variance associated with minVAR's representation of points on the Eulerian grid. (e) minVAR's maximum of two adjacent occupied cells per dimension was found sufficient to pinpoint the coordinates of the point being represented (Section 3) at a level of resolution limited only by numerical precision.

The last property is reminiscent of an early method developed for analyzing the numerical calculation of hydrodynamic shocks in one dimension (von Neumann and Richtmyer, 1950). Their idea was to add artificial (and nonlinear) dissipative terms to the hydrodynamic equations so as to *broaden* the shock front discontinuity, a point singularity in 1D, to "a thickness comparable to, but preferably somewhat larger than the spacing of the points of the network" used in their model. The effect was to make locating the shock singularity immediately evident as it moved through the fluid.

Most advection schemes in common use introduce nonlinearity at some stage of the process (Section 1). Errors during advection of independent tracers for which these schemes were designed are usually tolerable, but once even a small error enters into an interrelated tracer set it grows exponentially to infect other members of the set and information available at the start of the simulation is destroyed. The problem is discussed in Lanczos (Lanczos, 1988) and gets worse the higher the order of the scheme (Wright, 2007). Exponential error amplification during finite differencing is illustrated for a sequence of six moments from a lognormal distribution in (McGraw, 2012). Similar considerations are important when selecting a microphysical module to update aerosol and cloud particle properties between advection steps. Modal, moment, particle-resolved, and quadrature-based methods, all of which perform well as box models for updating the contents of a grid cell between advection steps, should be fully compatible with minVAR. An interesting question for future research concerns the extent to which minVAR can be used to reduce numerical diffusion in bin-sectional models of aerosol and cloud microphysical processes, a well-known problem especially for particles undergoing condensational growth. Unfortunately, microphysical processes tend to be nonlinear, making this last problem more difficult than the (inherently linear) advection of passive tracer.

In summary, a linear diffusion limiter has been developed and applied to the basic advection scheme. The new result (minVAR) has been found to be non-diffusive, non-dispersive, preservative of tracer set correlations, and capable of tracking sub-grid information at arbitrarily fine scales with high computational efficiency. These new capabilities should considerably advance progress toward achieving high-fidelity representations of aerosols and clouds in atmospheric transport models.

Appendix A

A1. Reversible Shear Flow

This section highlights the flexibility of minVAR-LP to handle irregular grids with cells of varying size and shape, and stability under variable conditions including Courant numbers greater than unity. Specifically, we consider the application of minVAR to all aspects of a textbook cylindrical flow problem, beginning with the generation of Lagrangian trajectories obtained from solutions of Navier-Stokes (NS) equations, through to the

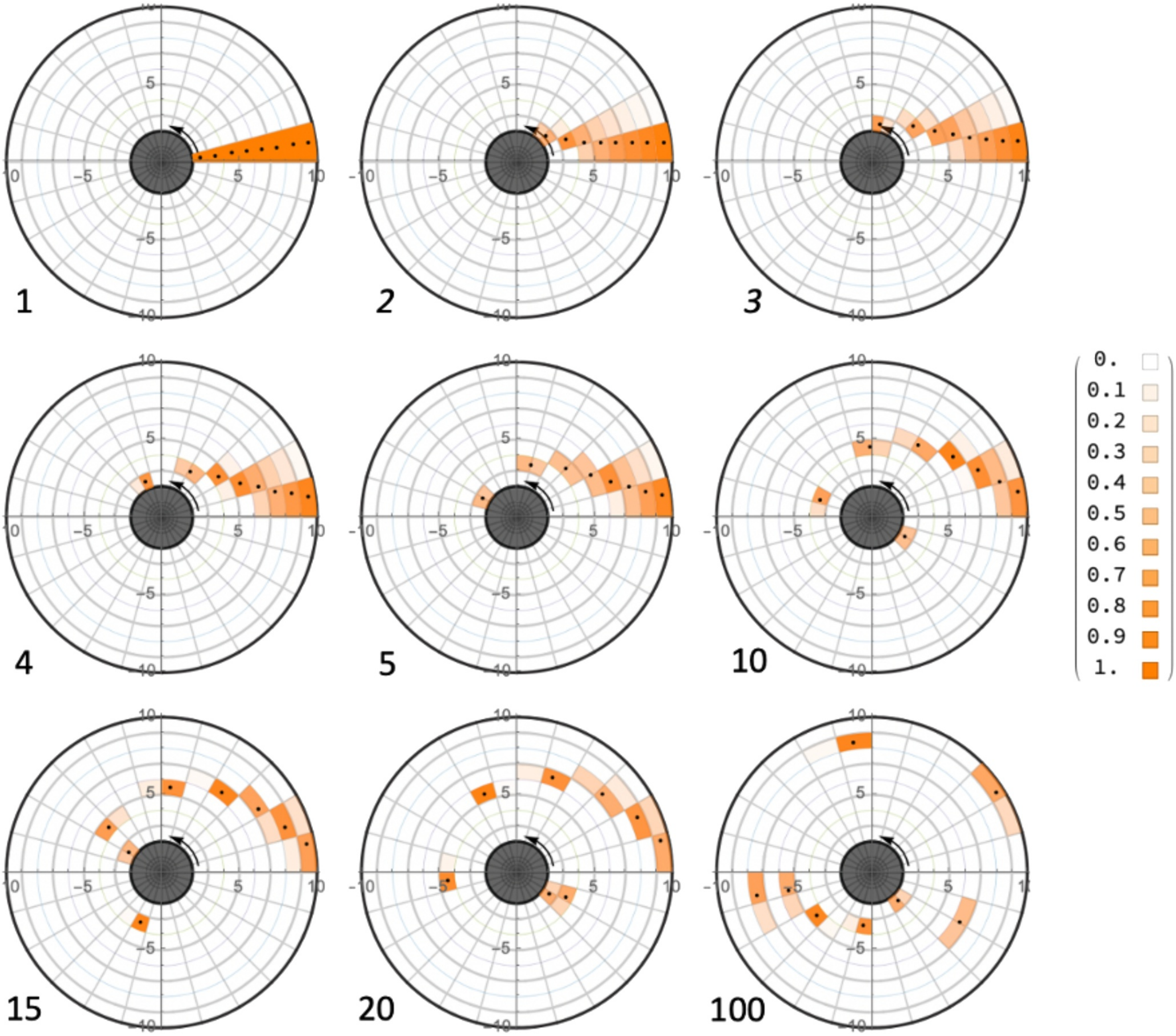

Figure A1. Comparing Lagrangian (black points) and Eulerian (shaded orange regions) representations for the circular advection of tracer under no-slip boundary conditions and laminar flow. Points evolve along constant radials, in a counterclockwise direction following Equations A1 and A2. Orange shadings show the distributions of normalized tracer mass, obtained using minVAR-LP. Colorscale values are shown in the legend. Numbers refer to the advection timestep with step 1 being the initial condition. Flows are reversible, with initial and intermediate conditions perfectly restored, on change of direction of inner cylinder rotation.

application of minVAR-LP to map points from these trajectories to a cylindrical Eulerian grid. The case under consideration treats the transport of fluid (air or liquid) in the annular region between the two coaxial cylinders sampled over 100 time steps, Figure A1.

We first require the flow velocity $V(r)$ where r is radial distance from the common axis. For the inner cylinder, located at $r = a$, $V(a) = a\Omega$ where Ω is angular velocity (radians/s), which we set to unity. For the stationary outer cylinder, located at $r = b$, $V(b) = 0$. The full solution, for no-slip boundary conditions, is available in Paterson and used here to locate points along eight distinct Lagrangian trajectories (Paterson, 1983):

$$V(r) = -\Omega\, a^2\, r/\left(b^2 - a^2\right) + \Omega\, a^2\, b^2/\left[\left(b^2 - a^2\right) r\right]. \tag{A1}$$

See (Heller, 1960) for a laboratory treatment of the same problem focused on reversibility and demonstration of unmixing*. Division by r gives the corresponding angular velocity:

Table A1
Mapping Radial Grid Circles From Orthographic Projection to Latitudes on the Hemisphere

Radii in outer grid	Latitude on sphere	Radii in inner grid	Latitude on sphere
0.3	72.5425	0	90 (north pole)
0.4	66.4218	0.025	88.5676
0.5	60	0.05	87.134
0.6	53.1301	0.075	85.6988
0.7	45.573	0.1	84.2608
0.8	36.8699	0.15	81.3732
0.9	25.8419	0.2	78.463
1.0	0 (equator)		

$$\Omega\,(r) = V(r)/r = -\Omega\, a^2\,/\left(\,b^2\; - a^2\right) + \Omega\, a^2\, b^2/\left[\left(\,b^2\; - a^2\right) r^2\;\right]. \tag{A2}$$

To illustrate we set $a = 2$ and $b = 10$ in the calculations used to generate Figure A1. With this assignment angular velocities range from 0.625 ($r = 2.5$) to O.00450139 ($r = 9.5$) with corresponding Courant numbers ranging from 2.38732 to 0.017*194*.

The first term on the right hand side of A2 describes a constant, r–independent, angular velocity, which if present alone would represent rigid body rotation. The second term allows for inclusion of shear and vorticity in the simulations. The no-slip boundary conditions, $\Omega\,(a) = \Omega$ and $\Omega\,(b) = 0$, result in flow deformation from shear and a lowering of the interior fluid pressure, P, with approach to the inner cylinder (Paterson, 1983):

$$dP/dr = \rho V^2/r \tag{A3}$$

where ρ is fluid density. Equation A3 ensures that the inward pressure gradient and outward centrifugal forces are in balance, as characteristic of stable vorticial flows. As a result there is no component of flow velocity along the radial coordinate. Accordingly, the one-dimensional linear program LP_{1D} is sufficient to map the Lagrangian

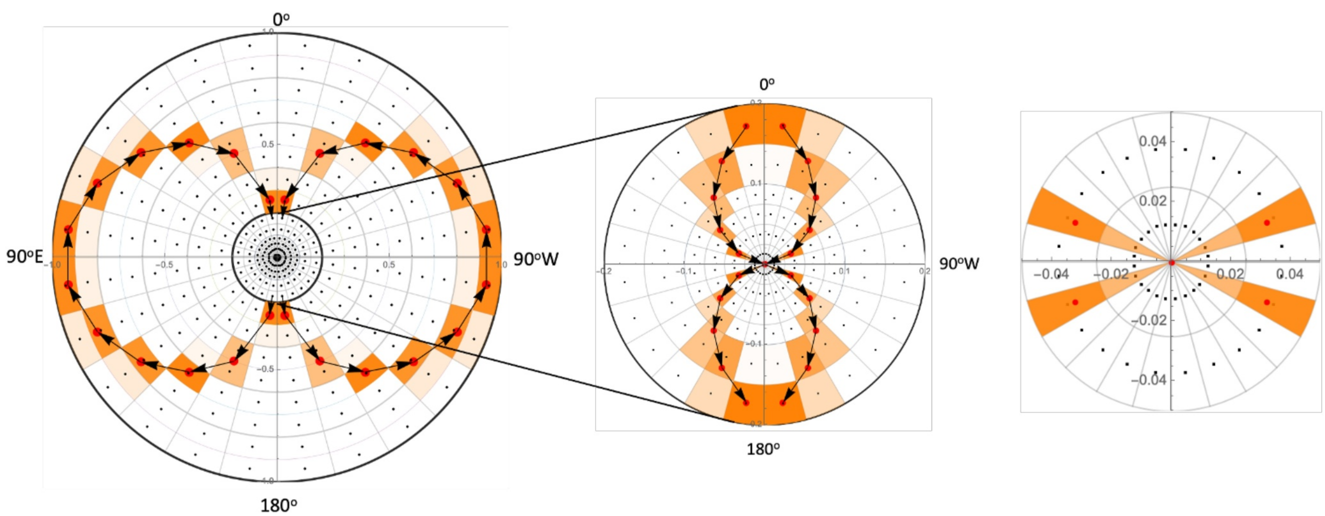

Figure A2. Lagrangian points (red dots) follow a figure-eight closed-loop trajectory centered at and twice crossing the pole. Arrows indicate the directions followed by the trajectory and shadings show the minVAR representation of these points on the grid. Each red dot is located at an angular midpoint between neighboring radials. Latitudinal values are arbitrary and were assigned to match values interpolated from Table A1. Black dots mark the grid centers (abscissas) used in the linear program and the shadings represent computed weights using the colorscale of Figure A1. As minVAR is free from numerical diffusion the path is identical from one cycle to the next, limited only by precision of the calculation. The region for latitudes above 78° (map radii less than 0.2), is enlarged in the middle figure. The four innermost arrows on the left figure show direction of tracer flux entering and leaving the high latitude region and connecting up with the arrows seen in the middle figure. Trajectory crossing occurs (twice/cycle) at the pole, as shown in the enlarged figure on the right.

Table A2
Degrees North (Latitude), East or West (Longitude) for Mapping Lagrangian Trajectory Points (Red Points in Figure A2) to the Surface of the Northern Hemisphere

Degrees N	Degrees E or W	Degrees N	Degrees E or W	Degrees N	Degrees E or W
20	82.5 E	75	172.5 W	90	Indeterminant
30	67.5 E	60	157.5 W	88	112.5 E
40	52.5 E	50	142.5 W	86	127.5 E
50	37.5 E	40	127.5 W	84	142.5 E
60	22. 5E	30	112.5 W	82	157.5 E
75	7.5 E	20	97.5 W	80	172.5 E
80	7.5 E	20	82.5 W	75	172.5 E
82	22.5 E	30	67.5 W	60	157.5 E
84	37.5 E	40	52.5 W	50	142.5 E
86	52.5 E	50	37.5 W	40	127.5 E
88	67.5 E	60	22.5 W	30	112.5 E
90	Indeterminant	75	7.5 W	20	97.5 E
88	112.5 W	80	7.5 W		
86	127.5 W	82	22.5 W		
84	142.5 W	84	37.5 W		
82	157.5 W	86	52.5 W		
80	172.5 W	88	67.5 W		

points in one-to-one correspondence to cells of the Eulerian grid—a continuance to non-uniform grids of the characteristic minVAR theme played throughout the present study. The computer code used to generate Figure A1 is available in the Open Research Statement.

* Reversibility and unmixing require the use of a viscous liquid between the cylinders (Heller used glycerin). For air a gaseous diffusion term would need to be added to the model, which is beyond the scope of this simple but illustrative test case.

A2. Hemispheric Scale Orthographic Projection of Flow Over the Pole

The grids and codes used to generate Figure A1 are easily adaptable to orthographic projection of Lagrangian trajectories to and from the surface of a sphere (here the northern hemisphere). Latitudes on the spherical surface are mapped to radial positions on the projection as shown in Table A1 for a sphere of unit radius. Several features of the calculation are worth noting: In passage from the equatorial region to the pole, resolution in the radial direction is first doubled, on entering the high-latitude region ($r < 0.2$), then doubled again closer to the pole ($r < 0.1$). The idea is to test for oscillations in tracer concentration associated with sharp resolution gradients in the grid. None were found, in accordance with Godunov's theorem that any linear algorithm for solving partial differential equations with the property of not producing new extrema can be at most first order. Both minVAR and the basic linear schemes satisfy this condition and are thus immune from nonmonotonicity and oscillatory effects.

A second feature of the calculation is that the Lagrangian points were chosen to lie at angular centers of the grid cells with latitudes arbitrary. In A.1 this situation is reversed with the Lagrangian points located at the radial midpoints and angular positions determined by fluid dynamics. The two grids were chosen this way to be complementary. In both cases a maximum of two grid cells are occupied, the calculations are effectively 1D, and the LP_{1D} program was used. For general placement of the Lagrange points (e.g., fully arbitrary trajectories over the sphere), up to four cells can be occupied and the LP_{2D} program used to fill the Eulerian grid. This was not done here to avoid crowding the figure.

The orange shadings of Figure A2 show the minVAR Eulerian representation for each of the points ordered along the Lagrangian trajectory listed in Table A2. Here the 1D form of minVAR-LP was used. The actual code itself is included as part of the Open Research Statement below.

Data Availability Statement

Computer codes for minVAR implementation and figure generation are available at https://zenodo.org/doi/10.5281/zenodo.7607751. All analyses were preformed using *Mathematica* Version Number 12.2.0.0.

Acknowledgments

R. McGraw (BNL) and F. Yang (BNL) acknowledge the Atmospheric Systems Research (ASR) Program of the U.S. Department of Energy (Grant DE-SC0012704) for financial support. L. M. Fierce (PNNL) is supported by the U.S. Department of Energy Office of Science Biological and Environmental Research as part of the Atmospheric Systems Research (ASR) Program. Pacific Northwest National Laboratory is operated by Battelle for the U.S. Department of Energy under Contract DE-AC05-76RLO1830.

References

Bazaraa, M. S., Jarvis, J. J., & Sherali, H. D. (2010). Linear programming and network flows (Wiley, Hoboken) chapter 6.

Bott, A. (1989a). A positive definite advection scheme obtained by nonlinear renormalization of the advective fluxes. *Monthly Weather Review*, *117*(5), 1006–1015. https://doi.org/10.1175/1520-0493(1989)117<1006:apdaso>2.0.co;2

Bott, A. (1989b). Reply. *Monthly Weather Review*, *117*(11), 2633–2636. https://doi.org/10.1175/1520-0493(1989)117<2633:r>2.0.co;2

Chandrasekhar, S. (1943). Stochastic problems in physics and astronomy. *Reviews of Modern Physics*, *15*(1), 79–80. Appendix I, The mean and mean square deviation of a Bernoulli distribution. https://doi.org/10.1103/revmodphys.15.1

Heller, J. P. (1960). An unmixing demonstration. *American Journal of Physics*, *28*(4), 348–353. https://doi.org/10.1119/1.1935802

Lanczos, C. (1988). *Applied analysis, chap. 5*. (p. 313). Dover.

Lauritzen, P. H., Conley, A. J., Lamarque, J. F., Vitt, F., & Taylor, M. A. (2015). The terminator "toy" chemistry test: A simple tool to assess errors in transport schemes. *Geoscientific Model Development*, *8*(5), 1299–1313. https://doi.org/10.5194/gmd-8-1299-2015

Lauritzen, P. H., & Thuburn, J. (2012). Evaluating advection/transport schemes using interrelated tracers, scatterplots and numerical mixing diagnostics. *Quarterly Journal of the Royal Meteorological Society*, *138*(665), 906–918. https://doi.org/10.1002/qj.986

Lawson, C. L., & Hanson, R. J. (1995). Solving least squares problems (SIAM, Prentice-Hall, Englewood-Cliffs, New Jersey) chapter 23.

McGraw, R. (2007). Numerical advection of correlated tracers: Preserving particle size/composition moment sequences during transport of aerosol mixtures. *Journal of Physics: Conference Series*, *78*, 012045. https://doi.org/10.1088/1742-6596/78/1/012045

McGraw, R. (2012). Correcting transport errors during advection of aerosol and cloud particle moment sequences in Eulerian models. In L. M. Druyan (Ed.), *Climate models chapter 13* (pp. 297–310).

McGraw, R., & Saunders, J. H. (1984). A condensation feedback mechanism for oscillatory nucleation and growth. *Aerosol Science and Technology*, *3*(4), 367–380. https://doi.org/10.1080/02786828408959025

Ovtchinnikov, M., & Easter, R. C. (2009). Nonlinear advection algorithms applied to interrelated tracers: Errors and implications for modeling aerosol– cloud interactions. *Monthly Weather Review*, *137*(2), 632–644. https://doi.org/10.1175/2008MWR2626.1

Paterson, A. R. (1983). *A first course in fluid dynamics* (pp. 144–146). Cambridge University Press.

Prather, M. J. (1986). Numerical advection by conservation of second-order moments. *Journal of Geophysical Research*, *91*(D6), 6671–6681. https://doi.org/10.1029/jd091id06p06671

Rood, R. B. (1987). Numerical advection algorithms and their role in atmospheric transport and chemistry models. *Reviews of Geophysics*, *25*(1), 71–100. https://doi.org/10.1029/rg025i001p00071

Russell, G. L., & Lerner, J. A. (1981). A new finite-differencing scheme for the tracer transport equation. *Journal of Applied Meteorology*, *20*(12), 1483–1498. https://doi.org/10.1175/1520-0450(1981)020<1483:anfdsf>2.0.co;2

Shia, R.-L., Ha, Y. L., Wen, J.-S., & Yung, Y. L. (1990). Two-dimensional atmospheric transport and chemistry module: Numerical experiments with a new advection algorithm. *Journal of Geophysical Research*, *95*(D6), 7467–7483. https://doi.org/10.1029/jd095id06p07467

Shohat, J. A., & Tamarkin, J. D. (1943). The problem of moments (American Mathematical Soc., New York). (p. 8).

Staniforth, A., & Thuburn, J. (2012). Horizontal grids for global weather and climate prediction models: A review. *Quarterly Journal of the Royal Meteorological Society*, *138*(662), 1–26. https://doi.org/10.1002/qj.958

Strang, G. (1988). *Linear algebra and its applications* (3rd ed.). Thomson Learning, Inc. Appendix A.

van Leer, B. (2006). Upwind and high-resolution methods for compressible flow: From donor cell to residual distribution schemes. *Communications in Computational Physics*, *1*, 192–206.

von Neumann, J., & Richtmyer, R. D. (1950). A method for numerical calculation of hydrodynamic shocks. *Journal of Applied Physics*, *21*(3), 232–237. https://doi.org/10.1063/1.1699639

Wright, D. L. (2007). Numerical advection of moments of the particle size distribution in Eulerian models. *Journal of Aerosol Science*, *38*(3), 352–369. https://doi.org/10.1016/j.jaerosci.2006.11.011

Yang, F., Ovchinnikov, M., Thomas, S., Khain, A., McGraw, R., Shaw, R. A., & Vogelmann, A. M. (2022). Large-eddy simulations of a convection cloud chamber: Sensitivity to bin microphysics and advection. *Journal of Advances in Modeling Earth Systems*, *14*(5), e2021MS002895. https://doi.org/10.1029/2021MS002895

Yoon, C., & McGraw, R. (2004a). Representation of generally mixed multivariate aerosols by the quadrature method of moments: I. Statistical foundation. *Journal of Aerosol Science*, *35*(5), 561–576. https://doi.org/10.1016/j.jaerosci.2003.11.003

Yoon, C., & McGraw, R. (2004b). Representation of generally mixed multivariate aerosols by the quadrature method of moments: II. Aerosol dynamics. *Journal of Aerosol Science*, *35*(5), 577–598. https://doi.org/10.1016/j.jaerosci.2003.11.012

Zalesak, S. T. (1979). Fully multidimensional flux-corrected transport algorithms for fluids. *Journal of Computational Physics*, *31*(3), 335–362. https://doi.org/10.1016/0021-9991(79)90051-2